Predicting Degradation Mechanisms in Lithium Bistriflimide "Water-In-Salt" Electrolytes For Aqueous Batteries

Malaurie Paillot, Alan Wong, Sergey A. Denisov, Patrick Soudan, Philippe Poizot, Bénédicte Claude-Montigny, Mehran Mostafavi, Magali Gauthier, Sophie Le Caër

ChemSusChem

Research Article
doi.org/10.1002/cssc.202300692

Chemistry Europe
European Chemical Societies Publishing

www.chemsuschem.org

Special Collection

Predicting Degradation Mechanisms in Lithium Bistriflimide "Water-In-Salt" Electrolytes For Aqueous Batteries

Malaurie Paillot,[a] Alan Wong,[a] Sergey A. Denisov,[b] Patrick Soudan,[c] Philippe Poizot,[c] Benedicte Montigny,[d] Mehran Mostafavi,[b] Magali Gauthier,*[a] and Sophie Le Caër*[a]

Aqueous solutions are crucial to most domains in biology and chemistry, including in energy fields such as catalysis and batteries. Water-in-salt electrolytes (WISEs), which extend the stability of aqueous electrolytes in rechargeable batteries, are one example. While the hype for WISEs is huge, commercial WISE-based rechargeable batteries are still far from reality, and there remain several fundamental knowledge gaps such as those related to their long-term reactivity and stability. Here, we propose a comprehensive approach to accelerating the study of WISE reactivity by using radiolysis to exacerbate the degradation mechanisms of concentrated LiTFSI-based aqueous solutions. We find that the nature of the degradation species depends strongly on the molality of the electrolye, with degradation routes driven by the water or the anion at low or high molalities, respectively. The main aging products are consistent with those observed by electrochemical cycling, yet radiolysis also reveals minor degradation species, providing a unique glimpse of the long-term (un)stability of these electrolytes.

Introduction

Li-ion batteries, widely used in electronic devices and electric vehicles, operate using electrolytes based on a salt dissolved in polar aprotic solvents such as organic carbonates. These solvents allow a relative stability over a wide potential window (a few volts), which is one of the crucial parameters that have led to the development of Li-ion batteries over the past 30 years.[1] However, non-aqueous electrolytes present severe issues in terms of safety, environmental impact, and cost. Indeed, ester or carbonate-based solvents used in Li-ion batteries are highly flammable, while the salts are costly, often toxic or harmful, and unstable at high temperatures, leading to the release of toxic gases.[2,3]

Rechargeable aqueous systems, studied since the 1990 s[4], could tackle these issues if their energy density was not limited by the narrow stability window of water (1.23 V), which excludes the use of low potential and high potential negative and positive electrodes, respectively. Outside this window, water electrolysis irreversibly consumes electrons to produce O_2 gas at high potential (through the oxygen evolution reaction (OER): $2H_2O \rightarrow O_{2(g)} + 4H^+_{(aq)} + 4e^-$) and H_2 gas upon reduction of water at low potential (hydrogen evolution reaction (HER): $2H_2O + 2e^- \rightarrow H_{2(g)} + 2OH^-_{(aq)}$). However, in the past few years, the development of concentrated electrolytes[5,6] has led to renewed interest in aqueous systems. A novel family of aqueous electrolytes, referred to as water-in-salt electrolytes (WISEs)[7] or hydrate-melt electrolytes[8] – obtained by dissolving a large amount of salt in water – increases the potential window of aqueous electrolytes to more than ~3 V. Using 20 molal (molality: m, moles per kg) lithium bis(trifluoromethanesulfonyl)imide (LiTFSI, see chemical formula in Figure 1) aqueous solutions, Suo et al.[7] demonstrated for the first time the relevance of this concept. Since then, further widening of the stability window above 3 V has been achieved by combining different imide salts,[8] through mixed cation electrolytes,[9] and by molecular crowding strategies,[10] while other studies have been dedicated to understanding the thermodynamics, kinetics[11] and mechanisms at play in these electrolytes.[12–16]

The degradation processes of water and salt seem to play a crucial role in the stability of WISEs. The concomitant lowering of the water content and the increase of the LiTFSI salt content upon the molality rise leads to the formation of a solid electrolyte interphase (SEI) layer that eventually restrains further

[a] M. Paillot, Dr. A. Wong, Dr. M. Gauthier, Dr. S. Le Caër
Université Paris-Saclay
CEA, CNRS, NIMBE
CEA Saclay, 91191 Gif sur Yvette Cedex (France)
E-mail: magali.gauthier@cea.fr
sophie.le-caer@cea.fr

[b] Dr. S. A. Denisov, Prof. M. Mostafavi
Institut de Chimie Physique UMR8000
CNRS, Université Paris Saclay
Bâtiment 349, 91405 Orsay (France)

[c] P. Soudan, Prof. P. Poizot
Nantes Université
CNRS, Institut des Matériaux de Nantes Jean Rouxel, IMN
Nantes, F-44000 (France)

[d] Dr. B. Montigny
Laboratoire de Physico-Chimie des Matériaux et des Electrolytes pour l'Energie (EA 6299)
Université de Tours
Parc de Grandmont, 37200 (France)

Supporting information for this article is available on the WWW under https://doi.org/10.1002/cssc.202300692

Special Collection This publication is part of a Special Collection on Battery Research in Europe jointly organized by Battery 2030+ and Chemistry Europe. It features contributions in the framework of Battery 2030+ from scientists throughout Europe.

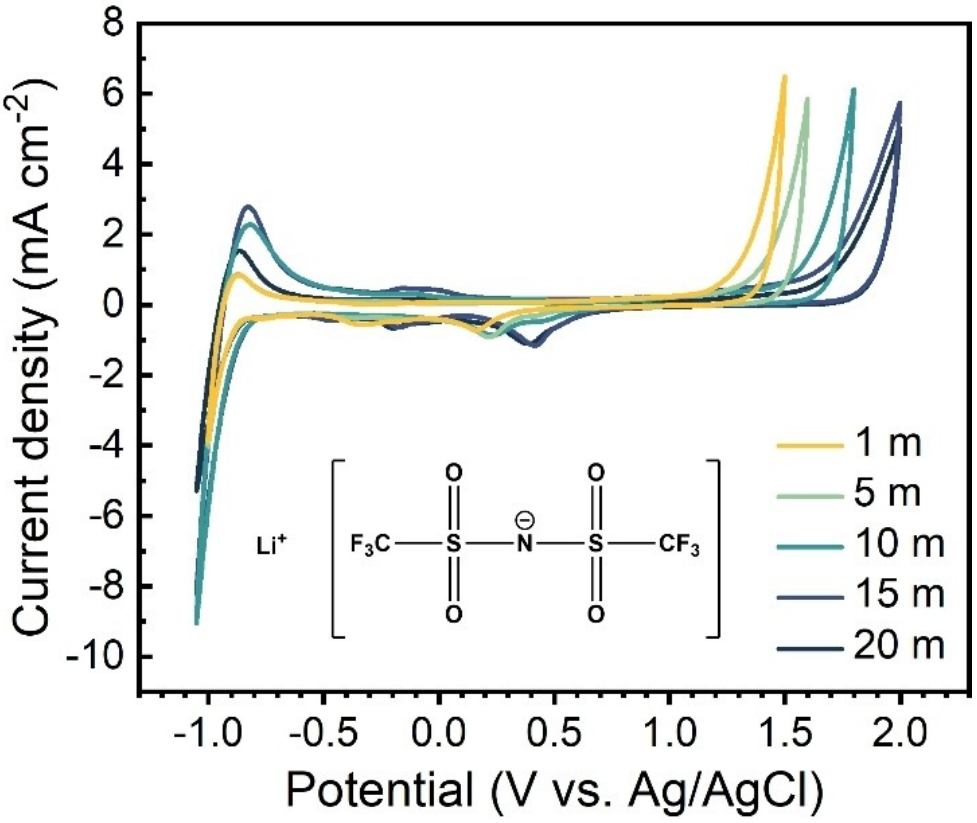

Figure 1. Cyclic voltammograms recorded in a three-electrode cell over a platinum working electrode with different LiTFSI-based electrolytes at 1 m, 5 m, 10 m, 15 m and 20 m recorded at a scan rate of 100 mV s^{-1}. The reference electrode is Ag/AgCl in a 3 M NaCl internal solution (1.95 V vs RHE) and the counter electrode is a platinum wire. The chemical formula of LiTFSI is also given in the figure.

water reduction.[12,17] On the oxidation side, raising the molality implies that negatively charged solvated anionic species accumulate at the electrode surface. They act as a hydrophobic anion-based double layer that drives off water molecules.[17]

While these impressive advances revived research into aqueous batteries, the practical viability of water-in-salt electrolytes is uncertain.[17] Their reactivity in the long term is scarcely known,[15–18] which calls for a deeper knowledge of the degradation reactions that may have a huge impact on battery performance. Usually, degradation investigations focus on the whole cell assembly with electrodes. Nevertheless, unraveling the degradation properties of the aqueous electrolyte itself is paramount and motivates the present study.

An unconventional technique, radiolysis, can evaluate the influence of water activity and the long-term (un)stability of electrolyte solutions and also provide kinetic data on the primary reactions at work during the aging of the electrolyte. Likened to "electrolysis without an electrode" by Marie Curie,[19] radiolysis can be used to simulate the electrolysis of an electrolyte inside a battery in a much shorter time, as already demonstrated for the accelerated aging of organic solutions used in Li-ion batteries.[20,21] Within a few hours, radiolysis can mimic the oxidation and reduction products from salt and solvent degradation (either in the form of a gas, liquid, or solid) that are only observed over the long operation of Li-ion batteries.[20–22] Importantly, for aqueous solutions, the radiolysis of water produces the same species as in electrolysis, such as H_2 and some radicals,[19] showing its ability to replicate degradation reactions in water-in-salt solutions.

While the LiTFSI salt is believed to be chemically and electrochemically stable,[23] we used radiolysis to understand the influence of water activity on the stability of aqueous LiTFSI-based solutions and to elucidate the degradation pathways that may prove essential to truly assess their behavior under long-term aging. Using picosecond-pulsed electron radiolysis, reactions involving solvated electrons are elucidated, revealing the effect of the salt concentration on the decay kinetics of the solvated electron. Lastly, a comparison between degradation species produced under radiolysis and electrochemical cycling is provided.

Results and Discussion

The main characteristics of the studied LiTFSI/water solutions are displayed in Table 1. LiTFSI solutions with water were prepared over a wide range of molalities (denoted as "m", and expressed in mol kg^{-1}) from 1 to 20 m, the latter value being just below the solubility limit (21 m at room temperature, see the experimental section).

Table 1. Characteristics of the different LiTFSI/water mixtures studied at 20 °C.

Solutions	LiTFSI concentration [mol L^{-1}] or ionic strength	H_2O/Li^+ molar ratio	Li^+/H_2O weight ratio	wt% (salt)	wt% (water)	Density at 293 K [g cm^{-3}]	Dynamic viscosity at 293 K [mPa s]
0.5 m	0.47	111.1	0.14	12.6	87.4	1.07	1.2
1 m	0.88	55.5	0.29	22.3	77.7	1.12	1.4
5 m	2.91	11.1	1.44	58.9	41.1	1.42	4.1
7 m	3.48	7.9	2.01	66.8	33.2	1.50	5.9
10 m	4.09	5.6	2.87	74.2	25.8	1.58	10.2
15 m	4.72	3.7	4.31	81.2	18.8	1.67	24.7
20 m	5.10	2.8	5.74	85.2	14.8	1.72	62.9

Determination of the electrochemical stability windows of the various electrolytes

The electrochemical stability window (ESW) of an electrolyte is dependent on the reduction and oxidation reactions of the electrolyte constituents at the surface of the electrode,[24] i.e., LiTFSI and water in the systems studied herein (Table 1). In the case of an aqueous electrolyte, the ESW is limited in reduction by the Hydrogen Evolution Reaction (HER) and in oxidation by the Oxygen Evolution Reaction (OER). These two reactions theoretically limit the ESW at 1.23 V for pure water.[25] In water-in-salt electrolytes, the native water stability window is significantly widened. The window extends with the molality, which is correlated with the role of the $TFSI^-$ anion and the alteration of the water molecule network.[12,14,24,26] The cyclic voltammograms for solutions of 1, 10, 15, and 20 m LiTFSI in water shown in Figure 1 confirm the increase of the electrochemical stability window when decreasing the H_2O/Li^+ molar ratio.[7,12,24]

As previously reported, a significant shift of the offset of oxidation occurs when molality is raised (Table S1).[7,12,24] In contrast, the reduction potential of the electrolyte does not change significantly when changing the molality. The same trends were observed for a glassy carbon working electrode (Figure S1 and Table S2 in the Supporting Information), but with wider electrochemical stability windows due to cathodic and anodic overpotentials linked to kinetics. The ESWs are narrower with Pt due to its catalytic nature in contrast to glassy carbon. When the molality reaches the maximum solubility of LiTFSI, the number of free water molecules able to react in the solution is very limited. The ESW limit is then defined by the reactions of other species, such as those implying the $TFSI^-$ anion, rather than the redox reactions of water.[7] Overall, the electrochemical stability windows shown in Figure 1 denote the change in the solvation behavior of the solutions and the strong influence of the reactivity of both water and $TFSI^-$ anions. These reactivity changes should strongly affect the degradation mechanisms of the solutions in the long term.

Characterization of the electrolytes

A prerequisite for understanding the degradation reactions of aqueous solutions as a function of their salt content is the knowledge of the changes undergone by the water H-bond network upon increasing molality. It can be assessed through FTIR and ^1H NMR experiments (Figure S2) and will be discussed briefly hereafter in light of data from the literature (see SI for more details).[14,26–30]

The evolution of the O–H stretching band upon raising the molality (Figure S2a) depicts well the interaction of water molecules with the salt. The intensity of the band decreases when molality increases, and its maximum is shifted towards a higher wavenumber, indicating an overall weakening of the H-bond network,[31] disrupted by the presence of the ions,[32] as already reported in the literature.[26] Moreover, the decrease of the half width at half maximum (HWHM) of the band when molality increases indicates that the variety of H-bond environments around water diminishes. This region can be decomposed with a combination of three contributions illustrating the H-bond interactions (Figure S3), as proposed in the work of Zhang et al.[14] Similar to what Zhang et al.[14] observed, at low molalities, most of the water molecules are in a state close to bulk water. When reaching molalities of 10 m, the infrared spectra are dominated by water molecules donating one or two H-bonds to $TFSI^-$ anions. Noticeably, when approaching the solubility limit of 20 m, the component (2w) representing the completely "free" water molecules has no contribution to the spectrum (Figure S3), emphasizing the strong change in the water network.[14]

The main bands of the $TFSI^-$ anion are depicted in Figure S2c. They are known to be located below 1400 cm^{-1}.[33] The intensity of the bands increases with molality; the bands observed between 1300 and 1400 cm^{-1} are assigned to the out-of-phase (contribution at 1327 cm^{-1}) and in-phase combination (contribution at 1350 cm^{-1}) of the antisymmetric stretching modes of both -SO_2 groups.[30] The component absorbing at the lowest wavenumber increases more with molality than at the highest. Lewis et al.[30] stressed that the broadening of these bands upon molality can be attributed to Li^+-$TFSI^-$ contact ion pairs.

Liquid ^1H NMR spectra were also recorded on the as-prepared solutions as a function of the molality (Figure S2d).

The ^{1}H signal is shifted to lower chemical shift values when the molality increases, in agreement with the findings of Dubouis et al.[12] This trend is due to the change in H-bonding interactions, water-water interactions being replaced by water-anion ones when molality rises.[12] The shift observed could also indicate some stronger interaction between water molecules and the cations, influencing the water reduction kinetics (Volmer step or water dissociation step: $H_2O + e^- \rightarrow H_{ads} + OH^-$)), explaining thus the weak influence of the molality on the reduction potential (Figures 1 and S1).

Globally, the behavior of these electrolytes can be understood as the following, based on Figure S2 and literature data:[26–30] when molality increases, water-water interactions are disrupted and replaced by anion-water ones. At high molality, a network containing the ions is found. In this network, anions are close to each other, with some Li^+ cations. Some authors have also proposed that these ions form a porous network in which nanometric water channels are found.[28]

Evaluating degradation mechanisms by radiolysis

Picosecond pulse radiolysis

In order to understand how the organization of water in concentrated LiTFSI-based solutions affects their reactivity, radiolysis experiments mimicking aging phenomena were carried out. First of all, to study the fate of the solvated electron in these electrolytes (ps-µs timescale), time-resolved pulse radiolysis experiments were performed. We focused on the solvated electron, a well-known precursor of H_2, a molecule of particular interest in samples subjected to aging[34] for the case of aqueous electrolytes, as H_2 is produced electrochemically from water reduction.

Neat water and LiTFSI solutions having a molality of 1, 7, 15, and 20 m were investigated. The corresponding spectra are displayed in Figure 2a. In the case of water, the broad spectrum with a maximum of 715 nm is characteristic of the hydrated electron.[35] Note that the upper wavelength was around 720 nm in the experimental configuration used in this work. When the solution contains LiTFSI, and when the molality rises, the shape of the band is globally unchanged, which implies that it can still be attributed to the hydrated electron. However, it shifts towards a lower wavelength when molality increases (Figure 2a and Figure S4a; see also the normalized spectra of the solvated electron, with the energy expressed in cm^{-1} in Figure S4b). Such a shift was already reported in concentrated solutions, for instance in Cl-based salts.[36] However, in this study,[36] the energy shift of the maximum of the band of the hydrated electron was significantly lower than what we detect here. For instance, the authors reported an energy shift of 0.13 eV for a 10 m LiCl solution, whereas a roughly 0.3 eV shift occurs for a 10 m LiTFSI solution (Figure S4a). Indeed, the nature of the anion affects the magnitude of the blue shift.[36] The blue shift increases with molality and reaches a plateau near the solubility limit (Figure S4a). Recent simulations have shown that this blue shift extension with molality can be attributed to an increased number of cations (Li^+ here) interacting with the electron.[37] Simulations also indicated that water molecules remain around the electron and the cations, even at the highest molalities.[37] It implies that Li^+ cations are surrounded by water molecules, even at the highest molality, which is consistent with previous molecular dynamics simulations.[27] Indeed, at 20 m, a high fraction (40 %) of Li^+ ions have no anions in their first coordination shell, the solutions being rather described as a 3D percolating Li^+-water network.[27]

Interestingly, time-resolved measurements show that in the case of the 15 and 20 m solutions, the maximum of the observed absorption band decreases to lower wavelengths before being stabilized (Figure 2c and Figure S5). The observed shift of the position of the band is around 20 nm and 35 nm for the 15 and 20 m samples, respectively. This process takes place with a characteristic time of 55 ps in the 20 m sample, whereas it is slightly shorter (around 46 ps) in the 15 m sample (Figure S5). This phenomenon is typical of the solvation of the electron, and the general process is accompanied by a global narrowing of the band (Figure 2c), as already reported for instance in ethylene glycol, a viscous solvent.[38] In ethylene glycol, it corresponds to corresponds to a long-range reorganization in a viscous and protic medium, reflecting the diffusive part of solvation.[38] It is also well described by the different kinetics measured at two different wavelengths; one in the tail of the band (725 nm) and the other around the maximum (575 nm, Figure 2b). Obviously, the trend is not the same within the first tens of ps on these curves, with an increase of the absorbance at 575 nm and a decrease at 725 nm. At 293 K, the dynamic viscosity was measured as 25 mPa s for the 15 m LiTFSI solution and around 63 mPa s for the 20 m sample (Table 1). Therefore, in a more viscous sample, a global slow-down of electron solvation is expected, as reported here (Figure S5). For comparison, solvation occurs in 50 ps in ethylene glycol, for a dynamic viscosity of 16 mPa s.[38] Assuming a linear behavior between bulk viscosity and solvation time, the solvation time was estimated by Steinrück *et al.* to be about 100 ps in a 21 m LiTFSI solution.[39] The value measured here is of this order of magnitude, although slightly smaller than expected. This may be due to the peculiar microscopic structure of the highly concentrated samples with ions forming a porous network in which nanometric water channels are found.[28] For lower molalities, solvation becomes faster and faster and can thus not be observed within the time resolution available.

The decay kinetics of the hydrated electron are displayed in Figures 2d-e, at the 10 ns and at the µs timescale, respectively. The kinetics presented on the 10 ns scale were normalized for the purpose of comparison (Figure 2d), but absorbance at $t = 0$ at the maximum of the band was higher for the 1 m sample than for the 20 m one (0.44 vs 0.195, respectively). Absorbance at $t = 0$ decreases when molality increases, as expected for a sample containing fewer water molecules. From the value of this absorbance, the $G(t) \times \varepsilon_{e\text{-}(aq)}$ value (for $t = 10$ ps) can be obtained, where $G(t)$ is the radiolytic yield of the solvated electron and $\varepsilon_{e\text{-}(aq)}$ is the molar extinction coeffievient at the maximum of the band (see the section "Calculation of the $G(t) \times$

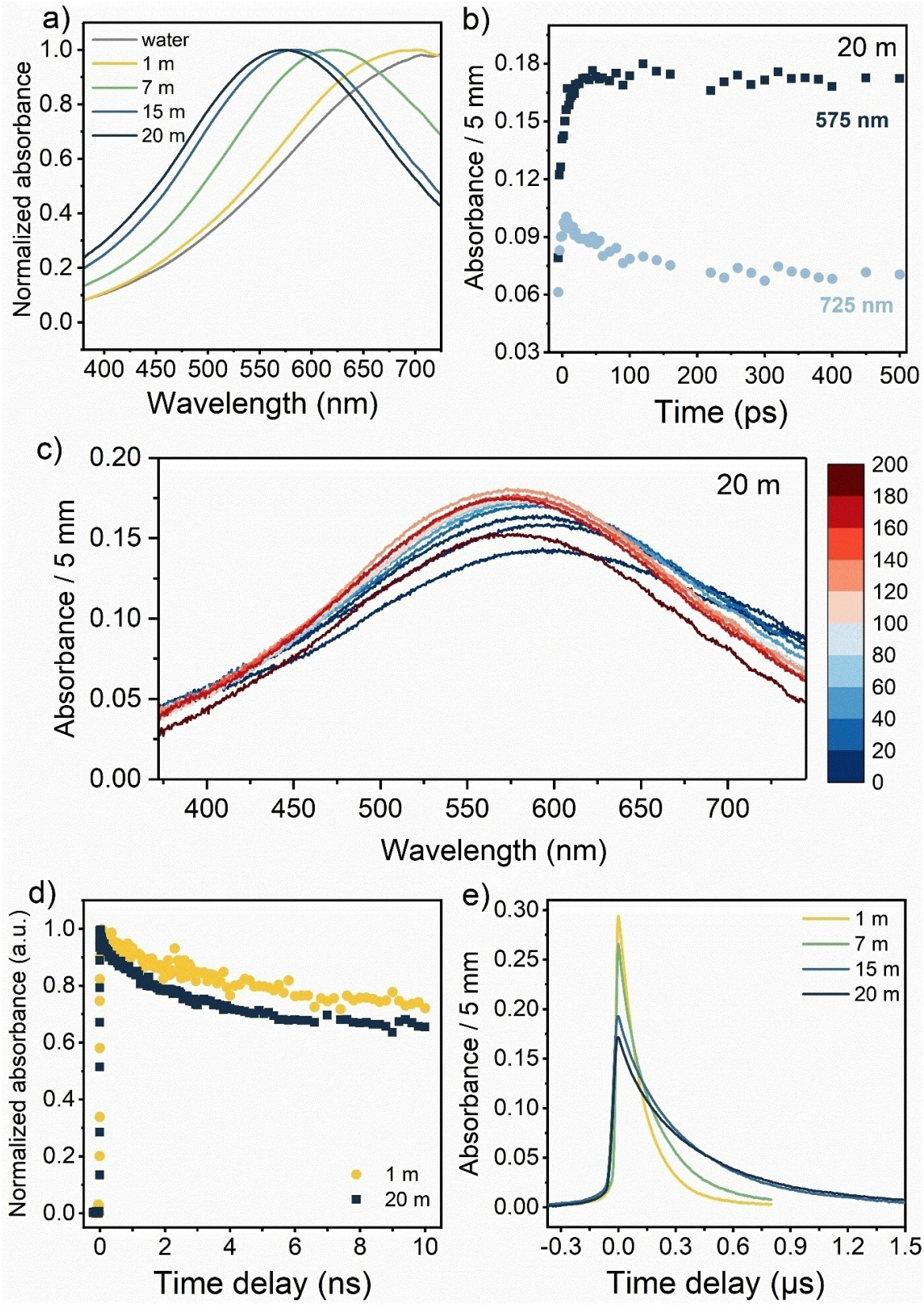

Figure 2. (a) Normalized optical absorption spectra of hydrated electrons in pure water and in aqueous LiTFSI-based electrolytes. (b) Kinetics measured for the 20 m solution at 575 and 725 nm. The dose per pulse was 105 Gy. (c) Evolution of the spectra measured during the first 200 ps in the 20 m solution. The dose per pulse was 105 Gy. The color bar indicates the times (in ps) at which the spectra were recorded. (d) Normalized decay kinetics measured on the 10 ns timescale for the solvated electron in 1 m and 20 m TFSI-based solutions. (e) Decay kinetics of the hydrated electron measured in the various LiTFSI electrolytes. The dose per pulse was 125 Gy. The value of the absorbance is given at the maximum of the band of the hydrated electron in each sample. Measurements were performed at room temperature (293 K).

$\varepsilon_{e\text{-}(aq)}$ value (for $t = 10$ ps) from pulse radiolysis experiments" in the Supporting Information, Table S3). We can consider that the oscillator strength of the solvated electron remains constant independent of the medium[40,41] (with a value around 1). It is proportional to the product of the width at half maximum of the solvated electron band and of the value of its molar extinction coefficient at the maximum of the band.[41] At room temperature, the width at half maximum of the band of the solvated electron is equal to 0.84 eV,[42] and it increases with molality (Figure S4b). Indeed, it was found to be around 0.90 eV for a solution at 7 m, and equal to 0.95 eV and 1.00 eV for solutions at 15 and 20 m, respectively. This implies then that the molar extinction coefficient of the solvated electron at the maximum of the band decreases when molality increases. Clearly, the $G(t)\times\varepsilon_{e\text{-}(aq)}$ value we measure decreases when molality increases (see Table S3 in the Supporting Information). However, the pronounced decrease of this value upon increasing molality also suggests that the radiolytic yield of the solvated electron decreases when molality increases.

The normalized decay kinetics of the solvated electron on the ns time scale are given in Figure 2d. In this time range, reactions within the spurs (i.e., regions of high concentration of chemical species after ionizing radiation had passed through) are measured. Obviously, the decay kinetics are faster at the highest molality, i.e., in the more viscous medium (Table 1). When viscosity increases, the reactions within the spurs are more favorable than the escape of the solvated electron into the solution, leading then to an enhanced decrease. In contrast, at the µs timescale, homogeneous kinetics are depicted (Figure 2e; see also the corresponding normalized decay kinetics in Figure S6). The decay becomes then slower when molality increases (Figure S6), which is due to the increase of the viscosity of the medium (see Table 1). Moreover, the decay features also change (Figure S6), getting closer to a first-order reaction when molality increases, suggesting the formation of solvated electrons in various domains of water separated by anion-rich domains. Interestingly, Steinrück et al.[39] reported a faster decay of the solvated electron in an ionic liquid containing $TFSI^-$ in the presence of LiTFSI than without. The difference between their observations and ours may be linked to the presence of water molecules in our case.

Detection of stable gaseous products formed upon irradiation

After irradiation, the identification and, if possible, the quantification of stable molecules were carried out on the different LiTFSI solutions to provide insights into the degradation mechanisms of the electrolytes. Firstly, micro-gas chromatography (µ-GC) experiments were performed to identify and quantify some gases (H_2, CO, CO_2, and CH_4) that can be produced upon irradiation. In LiTFSI solutions, only H_2 and CO_2 gases were detected. The amount of each gas, normalized with respect to the mass of the samples, is reported as a function of the dose received in Figure S7. The amount of gas released evolves linearly with the dose (Figure S7). The slope of the line allows us to obtain the gas radiolytic yield value, expressed in $mol.J^{-1}$ (Table S4). It corresponds to the amount of gas produced per energy deposited in the matter. The H_2 and CO_2 radiolytic yields are depicted on Figure 3 as a function of the salt molality.

Evidently, H_2 detected in the LiTFSI solutions after irradiation can only arise from water molecules in the electrolyte solutions as there are no H atoms in the LiTFSI salt. Nonetheless, we also checked that the salt alone did not lead to any H_2 production upon irradiation. Globally, the H_2 radiolytic yield is expected to drop when molality increases due to a decrease in the water percentage in the electrolyte. This trend is observed in Figure 3, except for the two lowest molality values for which the H_2 yield first rises. It is well known that the radiolysis of ultra-pure water does not lead to dihydrogen formation.[34] Indeed, in pure water, H_2 builds up to a steady-state concentration at which the destruction rate is equal to its production rate. The radiation-induced destruction reaction is mediated by $HO^\bullet$ radicals. Therefore, $HO^\bullet$ radical scavengers are commonly added in ultra-pure water in order to allow the detection of H_2. In the present case, the salt itself (and especially the anion) certainly plays the role of $HO^\bullet$ radical scavenger, as significant H_2 production is always measured. This accounts for the increase of the H_2 yield at the lowest molalities when the amount of salt increases, the salt protecting H_2 from $HO^\bullet$ attack. Noteworthily, the H_2 production values measured at the lowest salt molalities, $(5.8\pm0.6)\times10^{-8}$ mol J^{-1} and $(7.1\pm0.7)\times10^{-8}$ mol J^{-1} for 0.5 and 1 m, respectively, are larger than the primary H_2 yield in water ($G_{H2} = 4.5\times10^{-8}$ mol J^{-1}).[34] These values suggest an efficient recombination between two hydrogen atoms and/or between two hydrated electrons, leading to the formation of H_2. Indeed, pulse radiolysis data evidence the fast decay kinetics of solvated electrons in the 1 m solution (Figure 2e).

Globally, a competition between LiTFSI as a $HO^\bullet$ radical scavenger and the amount of water molecules occurs. At the lowest molalities, the presence of salt prevails, whereas as the molality increases, the lower amount of water molecules leads to a decrease in H_2 radiolytic yield.

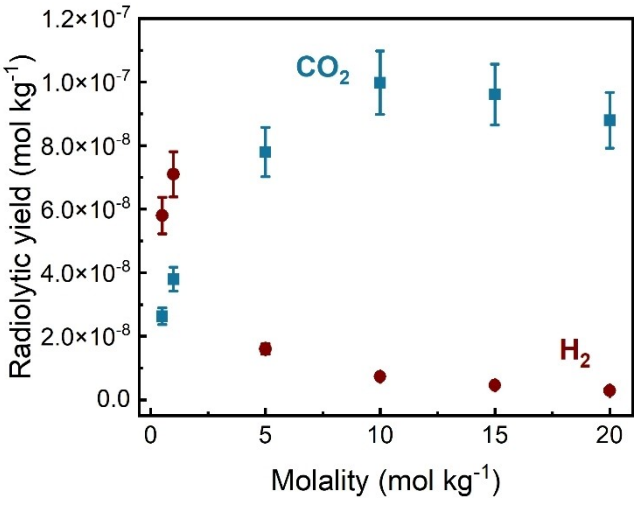

Figure 3. Evolution of the H_2 (red circles) and CO_2 (blue squares) radiolytic yields as a function of the molality of the LiTFSI-based solutions.

The trend in CO_2 production differs from that of H_2, as shown in Figure 3. Specifically, CO_2 production increases up to 10 m and then experiences a slight decrease. The $-CF_3$ groups in the anion are the sole carbon source in the samples, while the oxygen atoms in CO_2 may originate from sulfonyl groups and/or water molecules. However, no CO_2 was detected in the irradiated salt powder, suggesting that the origin of the oxygen atoms in carbon dioxide arises from water molecules only. Hence, the CO_2 production is influenced by both the water and the anion, implying that an optimal molality exists, resulting in a maximal release of carbon dioxide (around 10 m as shown in Figure 3). At a low molality, there are only a few carbon atoms available to react, leading to a low radiolytic yield of CO_2, while the yield increases upon raising the molality. However, the number of water molecules decreases at high molalities, implying a slight decrease in CO_2 production (refer to Table 1).

If we compare the H_2 and CO_2 radiolytic yields, the H_2 yield is the highest at low molality ($(7.1 \pm 0.7) \times 10^{-8}$ mol J^{-1} at 1 m), indicating, as expected, preferential water radiolysis. On the contrary, at high molality, the CO_2 radiolytic yield (around 10^{-7} mol J^{-1}) is higher than the H_2 one, denoting a significant degradation of the anion.

Interestingly, the commonly used discussion on direct vs. indirect effects in radiation chemistry (the most abundant part of the sample is directly affected by ionizing radiation) does not apply here. In this assumption, additivity of direct and indirect effects is assumed. The radiolytic yield for the formation of a given product (G) can be expressed by the following equation:

$$G = f_{salt} G_{salt} + (1 - f_{salt}) G_{water} \quad (1)$$

Where f_{salt} is the ratio of the energy directly absorbed by the salt to the total energy absorbed by the solution; and G_{salt} (G_{water}, respectively) the radiolytic yield of the given product after irradiation of the salt (of water, respectively) only. f_{salt} is roughly equal to the weight fraction of the salt in the sample. If we consider, for instance, CO_2 production, then G_{salt} and G_{water} are equal to zero, as they do not lead any to any carbon dioxide production. Water and LiTFSI are both necessary to generate CO_2. This means that an ideal additivity law is improper, as the interaction between both parts of the sample takes place. In the case of H_2, G_{salt} is equal to zero. Moreover, at the lowest values of f_{salt}, H_2 production is increased as compared to that measured in pure water, indicating again that the above equation is inappropriate. This highlights strong synergetic effects between water and the salt, making relations based on additivity not adequate to describe the behavior of the samples.

In order to determine the nature of the various gases that were produced upon ionizing radiation, gas chromatography coupled to mass spectrometry (GC-MS) experiments were carried out for LiTFSI aqueous solutions at two markedly different molalities: 1 m and 15 m (see Figure S8 for a global view of the chromatograms and Figure 4). It is important to note that the area of each peak is proportional to the concentration of the detected molecule. The experiments evidence the formation of numerous gases, showing the degradation processes at work in the samples. The retention times of the main products are given in Tables S4 and S5 for the 1 m and 15 m solutions, respectively. Obviously, from Figure 4, the degradation channels and gas amounts increase with molality.

Interestingly, the salt alone led to almost no gas production (Figure S9). Its color changes, however, upon irradiation, suggesting the formation of F-centers (electron color centers, Figures S10, S11). The behavior observed in the solutions again highlights that interactions between water and anions are responsible for producing many degradation compounds. The presence of some gases depends on the molality and hence, on the respective water/anion content and interaction. Thus, a species containing hydrogen atoms (arising from water only) such as H_2S is only detected for the irradiated 1 m molality solution (Figure 4a).

Similarly, species characteristics of the degradation of the anion, such as SO_2 or C_3F_8 are only detected in the most concentrated electrolyte (Figures 4b and c). Knowing that the salt does not lead to any significant gas formation (Figure S9), water plays a significant role in the degradation processes, even when present in low amounts. At both 1 and 15 m molalities, most gases formed contain -CF_3 groups, such as C_2F_6 (Figure 4a) and CF_3SCF_3 (Figure 4d). This suggests a C–S bond cleavage, leading to the formation of $CF_3^{\bullet}$ radicals. These radicals can react with themselves to form C_2F_6 or with water to abstract one hydrogen atom, leading then to HCF_3. Another class of detected compounds is CO_2 (whose formation was quantified by μ-GC, Figure 3), COS, and, at the highest molalities, SO_2, arising from the anion.

Degradation products detected in the liquid phase

NMR spectroscopy was employed on a 15 m LiTFSI solution irradiated at a high dose of 500 kGy to unravel degradation products that are soluble in the electrolyte solutions, in addition to the gases produced during irradiation. A high molality was chosen to better detect the degradation products arising from the anion.

Among the NMR-observable nuclei, the ^{19}F nucleus is a highly sensitive nuclear probe for fluorinated organic compounds. This arises from its 100% natural abundance with a large Larmor frequency and a large chemical shift range. The ^{19}F NMR spectrum of a non-irradiated 15 m LiTFSI showed a sole peak at −78.77 ppm ascribed to the $TFSI^-$ anion (data not shown). On the contrary, a vast number of low intensity peaks appear throughout the spectral range between −200 to +60 ppm (Figure 5 and Figure S12) in the sample irradiated at 500 kGy. The total sum of these peak integrals is $<1\%$ of the $TFSI^-$ peak integral. This renders the unambiguous assignment of these peaks difficult. A few peaks appearing at a highly deshielded region between 30–60 ppm could be assigned to $R–C(O)_xF_y$, $R–S(O)_xF_y$, and SF_6 species.[43]

The majority of the peaks are found around −90 to −60 ppm and particularly near the $TFSI^-$ anion peak,[44] suggesting that most of the radiolytic products are compounds

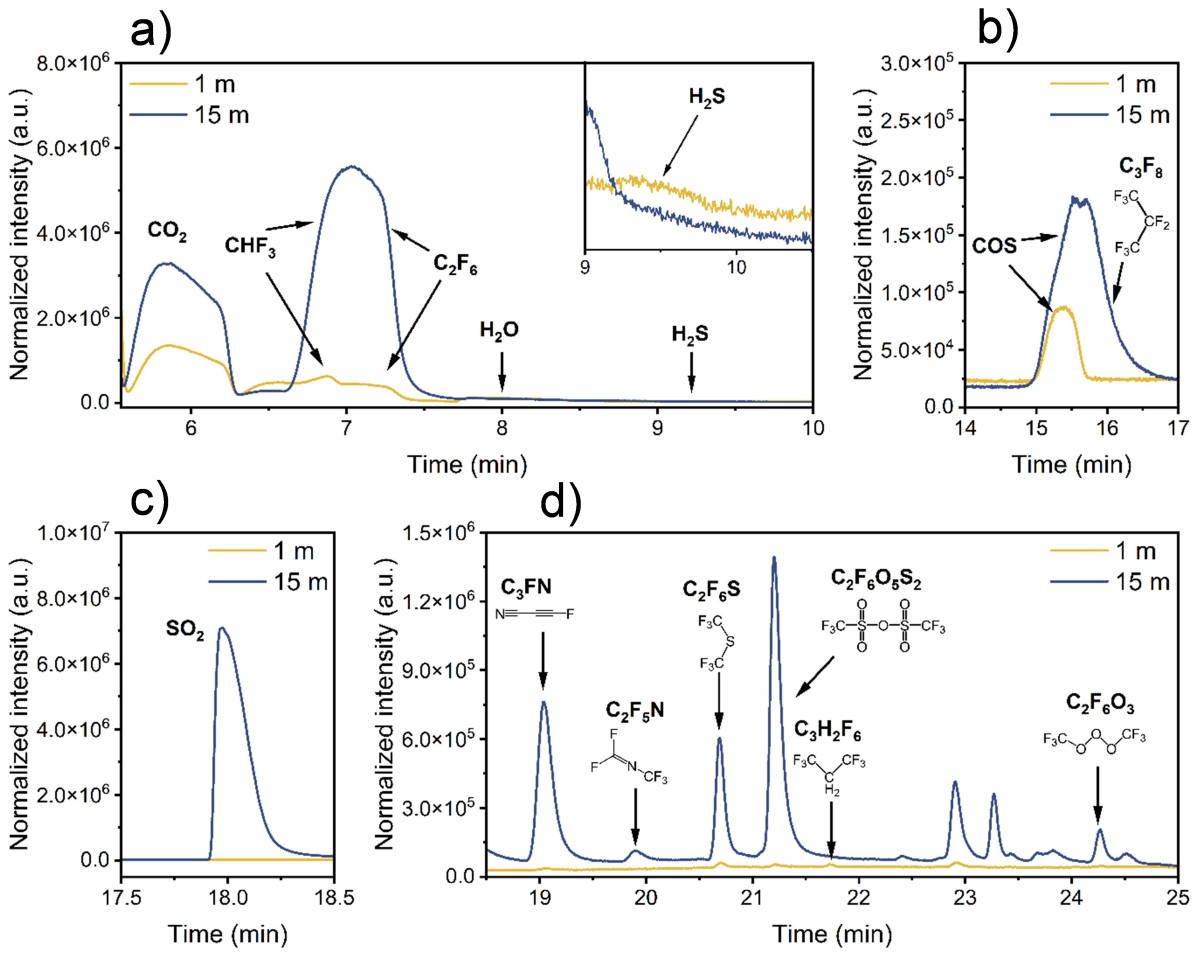

Figure 4. GC-MS chromatograms of gases produced after a 120 kGy electron irradiation of a 1 m and a 15 m LiTFSI-based solution. The species identified are indicated on the figures. (a–d) Correspond to magnified views of regions of interest on both chromatograms shown in Figure S8 (Supporting Information). The area of each peak is proportional to the concentration of the corresponding detected molecule.

based on sulfonic and -CF_3 groups including $(CF_3SO_2)_2O$ (−72.3 ppm), $CF_3SO_3CH_3$ (−74.8 ppm), $CF_3SO_2NH_2$ (−79.27 ppm), CF_3SO_2OH (−78.6 ppm), and CF_3SOO^- (−86.1 ppm) (see Table S7 for details).[43] Similar sulfonic-based products were previously identified by ^{19}F NMR from the radiolysis of [C_4mim][TFSI].[44] Based on the peak integral, $CF_3SO_2NH_2$ and CF_3SOO^- are the main NMR-observable radiolytic products. In the shielded spectral region, few anions are detected, including the pure fluoride peak at −124.2 ppm and HF_2^- at −153.0 ppm (Figure 5a).[44] A ^{19}F doublet signal at −122.5 ppm with a J-coupling of 55 Hz correlates well with the ^1H triplet at 6.3 ppm on the ^1H spectrum (Figure 5c), suggesting the possible presence of an alkyl species with a $-CF_2H$ group.[43]

Unlike the ^{19}F spectrum, the ^1H spectrum (Figure 5b) presents only three low-intensity peaks, in which the triplet at 6.3 ppm corresponds to the fluorinated alkyl compound $-CF_2H$, as detailed above. The strong signal at 6.6 ppm could be assigned to a sulfuric acid derivative like CF_3SO_2OH, while the weak peak above 8 ppm could be ascribed to HF and correlated to the ^{19}F peak around −153 ppm.[21] LiF was also detected (Figure 5c). Notably, the formation of these species was reported for a LiTFSI WISE/solid interface probed by synchrotron X-rays.[39]

Proposed reaction scheme

On the one hand, water radiolysis can be written as Eq. (2):[19]

$$H_2O \xrightarrow{\text{ionizing radiation}} e_{aq}^-, HO^\bullet, H^\bullet, H_3O^+, OH^-, H_2O_2, H_2 \quad (2)$$

The reactions accounting for the formation of H_2 in water are well documented, for example, from the reaction between two hydrated electrons.[34] The primary radicals produced during radiolysis of water are not very reactive towards $TFSI^-$,[39] which leads to fewer decomposition products and in smaller quantities when the molality of the salt is low.

On the other hand, the following reactions involving the anions subjected to ionizing radiation can be proposed based on our findings and literature data focusing on the radiation chemistry of ionic liquids possessing the same anion.[45–48] These processes are all the more important as molality increases. When the anion (the Li^+ cation being inert towards irradiation)

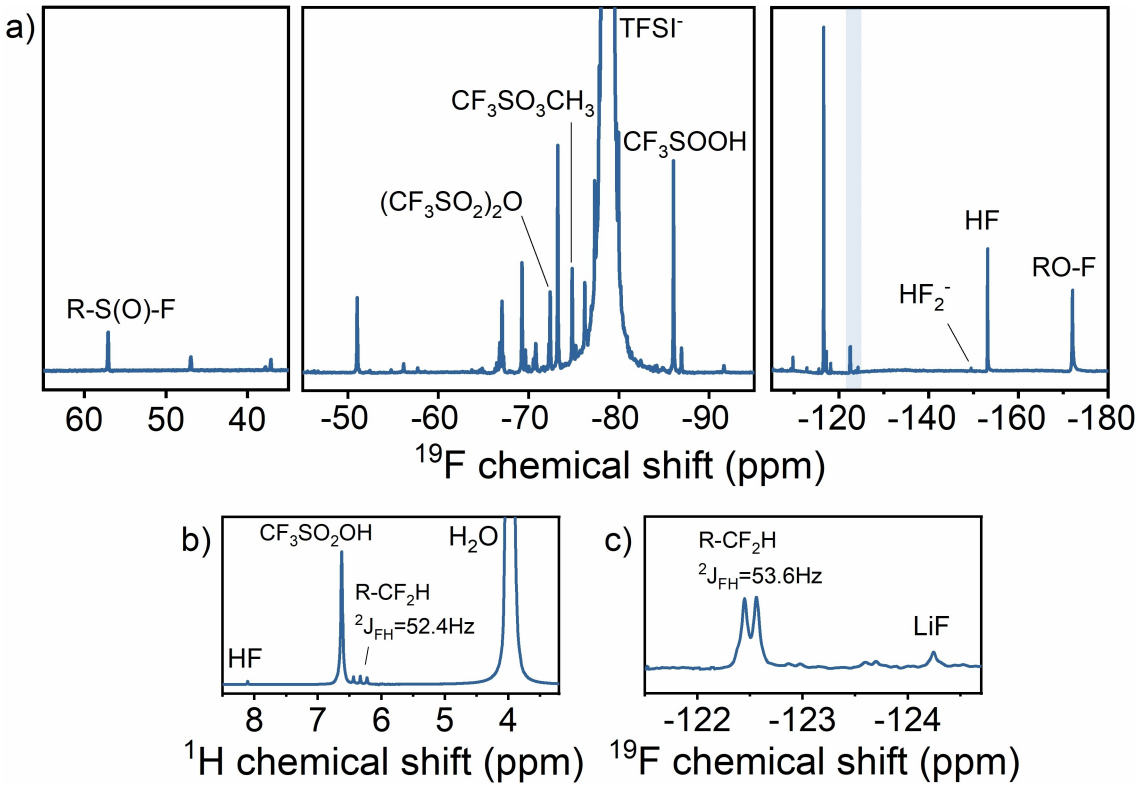

Figure 5. a) ^{19}F NMR spectrum of the 15 m LiTFSI solutions irradiated at 500 kGy. The spectrum is magnified by 500 to 5000 compared to the complete spectrum (Figure S12), showing the large predominance of the $TFSI^-$ anion on the spectrum. b) ^{1}H NMR spectrum of the 15 m LiTFSI solutions irradiated at 500 kGy. c) Magnified view of the blue region of the ^{19}F spectrum in a). Reference chemical shifts for products assignments are gathered in Table S7.

constitutes the major part of the sample, its direct interaction with ionizing radiation leads to excitation and ionization, producing an electron and a $TFSI^•$ neutral radical according to Eq. (3):[46,47]

$$TFSI^- \rightsquigarrow TFSI^{-*}, TFSI^•, e^- \quad (3)$$

Excited $TFSI^-$ can lead to the neutral radical and the electron[46] [Eq. (4)]. In the electronically excited state of $TFSI^-$ and in the neutral $TFSI^•$ radical, the S–N bond is cleft [Eqs. (5) and (6)]:[46,48]

$$TFSI^{-*} \rightarrow TFSI^• + e^- \quad (4)$$

$$TFSI^{-*} \rightarrow {}^{-•}NSO_2CF_3 + CF_3S^•O_2 \quad (5)$$

$$TFSI^• \rightarrow {}^•NSO_2CF_3 + CF_3S^•O_2 \quad (6)$$

After reaction with water, the $^•NSO_2CF_3$ radical can lead to the formation of $CF_3SO_2NH_2$, as observed by NMR (Figure 5 and Table S7).

The $CF_3S^•O_2$ radical can dissociate, forming the $C^•F_3$ radical together with SO_2 (Figure 4c) according to Eq. (7):

$$CF_3S^•O_2 \rightarrow C^•F_3 + SO_2 \quad (7)$$

NMR results (Figure 5) also suggest that these $CF_3S^•O_2$ radicals can react with water, leading to the formation of CF_3SO_2OH or CF_3SOOH species.

$C^•F_3$ radicals can then react with each other, leading to the formation of C_2F_6, C_3F_8, and longer C_xF_x molecules. It can also abstract one hydrogen atom from water molecules, leading to the formation of HCF_3. These radicals are very reactive, producing many products (Figure 4).

In the literature, another reaction is also reported, which corresponds to an electron attachment reaction, leading to the release of a fluoride anion, after the formation of a transient dianion.[46] However, this reaction is rather slow.[49]

$$TFSI^- + e^- \rightarrow {}^•CF_2SO_2N^-SO_2CF_3 + F^- \quad (8)$$

The formation of the fluoride anion is confirmed by NMR data (Figure 5). Noteworthily, under synchrotron X-rays, the surface-reduction of a LiTFSI-based WISE was reported to lead to the formation of LiF, in agreement with our findings,[39] while in contrast to this study, the reduction of LiTFSI to LiF was observed only at the interface with a solid. The fluoride anion is also observed as corrosive hydrofluoric acid (Figure 5). Besides the fluoride anion, the formation of a $^•CF_2$-type radical can account for the formation of RCF_2H species detected by NMR (Figure 5), after reaction with water. Moreover, ab initio molecular dynamics simulations have shown that a pre-solvated excess electron could attach to $TFSI^-$, leading to the formation

of a transient dianion. In this latter species, the N–S bond could then be cleft within the first 50 fs.[50]

In the case of CO_2 production, whose formation requires water and salt, the following reactions can be proposed. First, $C^{\bullet}F_3$ radicals react with $HO^{\bullet}$ formed in the radiolysis of water [Eq. (9)]:

$$C^{\bullet}F_3 + HO^{\bullet} \rightarrow CF_2O + HF \quad (9)$$

It was also shown recently by DFT-based molecular dynamics simulations that CF_3OH quickly loses its proton and that it could be the precursor of CF_2O in these WISE solutions.[51]

Carbonyl difluoride (CF_2O) is unstable in water. Its hydrolysis leads to the release of carbon dioxide [Eq. (10)]:[52]

$$CF_2O + H_2O \rightarrow CO_2 + 2HF \quad (10)$$

Of course, increasing molality (accompanied by a change in the environment of the water molecules) has a clear impact on the rate constants of the reactions described above. Thus, as observed in Figure 2e, the decay kinetics of the solvated electron are slower with increasing molality, due to the increased viscosity of the medium.

Comparing degradation mechanisms by radiolysis with electrochemistry

To assess the potential of radiolysis to mimic and predict electrochemical degradation mechanisms in WISEs, we compared the degradation products formed, and how they evolved with the solution molality, under both irradiation and during the cycling of full two-electrode cells. Ampoules similar to the ones used in radiolysis were specifically modified in order to enable electrochemical cycling tests and collect subsequently the gases (Figure S13). By playing on the balance between positive and negative electrodes and on the overall potential, one can promote either the OER (or oxidation) or HER reactions to favor either the oxidative and reductive degradations, respectively. Accordingly, an excess of the negative electrode (capacity ratio N/P (negative/positive) >1) was used to favor the oxidation of the solution through OER, for example, while the negative electrode was set as the limiting one (ratio N/P <1) to exacerbate the reduction of water through HER (see Figure S14 for details).

Figure 6a shows the cycling behavior of $LiMn_2O_4/Mo_6S_8$ full cells using stainless steel current collectors (ratio N/P$\approx$1:2) with 5 or 15 m LiTFSI aqueous electrolytes with a full cell

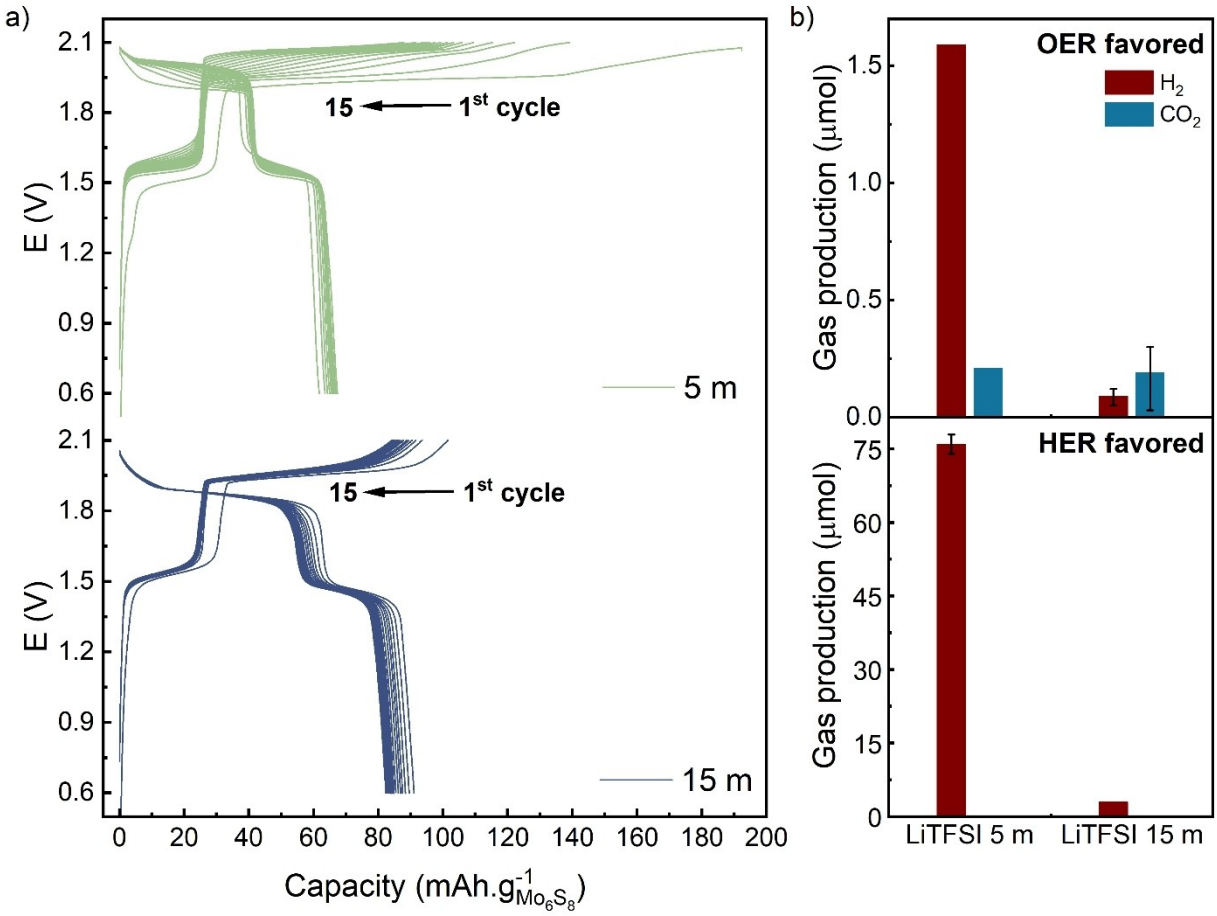

Figure 6. a) Galvanostatic cycling profiles of 5 m LiTFSI at the top and 15 m LiTFSI on the bottom with $LiMn_2O_4$ and Mo_6S_8 as a positive and negative electrode, respectively, at a rate of C/5 during 15 cycles with a full cell potential limited at 2.1 V and a ratio N/P <1. b) Gas production of H_2 and CO_2 after 15 cycles when oxidation is favored at the top and when the HER is favored at the bottom.

potential set at 2.1 V in charge. In that case, the water reduction is targeted as the limiting electrode is the negative one. The potential profiles of the full cells present two potential plateaus at around 1.6 V and 1.9–2.0 V, in agreement with previous studies.[53] The potential values of the plateaus match well with the potential difference expected between the characteristics plateaus of $LiMn_2O_4$ (4.3 and 4.1 V vs. Li^+/Li) and Mo_6S_8 (2.5 and 2.2 V vs. Li^+/Li) upon lithiation. The irreversibility of the cell is strongly dependent on the electrolyte molality. The first charge of the cell with the 5 m LiTFSI electrolyte (Figure 6a, top) presents a long plateau at a high potential corresponding to a large irreversible capacity due to water decomposition through HER, as the higher plateau corresponding to the complete lithiation of Mo_6S_8 cannot be reached.[53] Quantitative gas analysis performed after 15 cycles confirms the large water reduction and irreversibility with a large production of H_2 (Figure 6b, bottom), representing on average 76 μmol of H_2 and 59% of the total irreversibility of the cell if only the direct HER reaction is considered[17] ($H_2O + 1e^- \rightarrow HO^- + 1/2H_2$). O_2 is detected in a very low amount (~4 μmol) in contrast to a previous study from Suo et al.[53] where some O_2 gas was noticeably detected during the first cycle, even if to a lesser extent than H_2.

The behavior of the concentrated 15 m electrolyte is markedly different. The potential profile (Figure 6a, bottom) demonstrates good reversibility suggesting that water reduction at the negative electrode is strongly limited. This is supported by gas analysis after 15 cycles (Figure 6b, bottom) with an H_2 production that is strongly reduced (3 μmol), more than 20 times less than with the 5 m solution. Again, H_2 is the main gas detected, with O_2 representing less than 0.4 μmol, similar to what was observed by Droguet et al.[17] with a 20 m solution after a few cycles. The irreversibility caused by water reduction is estimated to be 40% of the total irreversibility. Of course, the quantitative values measured after radiolysis and cycling cannot be compared, while the evolution and trend can be and are discussed hereafter. The results shown in Figure 6 are consistent with those obtained by radiolysis, where the H_2 radiolytic yield decreases when molality increases from 5 to 15 m (Figure 3), although to a lower extent than here. It is interesting to note the strong inhibition of the H_2 production when increasing the molality at 15 m, while the HER onset potentials are almost not affected when moving from 5 to 15 m (Figure 1 and S1). This suggests the preeminence of kinetics factors compared to thermodynamics factors in the electrochemical behavior of the LiTFSI WISEs.

When considering a capacity ratio $N/P > 1$ to favor water oxidation (Figure S15, potential limited at 2.1 V), the release of O_2 is surprisingly low (0.36 μmol on average with 15 m), while H_2 is still present along with CO_2. The quantity of H_2 detected in that case is 30 times smaller than in the case where the HER is favored. Here again, and similar to the radiolysis experiments, H_2 production decays when molality is raised from 5 to 15 m. The limited release of O_2 compared to H_2 can be rationalized by some kinetic considerations, as the H_2 evolution is more kinetically favorable than the O_2 evolution.[54] Moreover, the oxidation limit of the 15 m solution for OER is very high and probably not completely reached. It is also probably explained by the release of CO_2 that may be produced by degradation mechanisms involving oxygen gas. Interestingly, the detection of CO_2 agrees with the results obtained by radiolysis, with, on average, an apparently slight increase of CO_2 production when molality increases from 5 m to 15 m (Figure 3). Only the mean trend for CO_2 can be discussed here as the quantities of CO_2 released fluctuate from one experiment to another. Note that CO_2 release from the carbon additive decomposition at high potential is a possibility that cannot be completely neglected.[55]

Apart from gas analysis, some NMR measurements were also performed on a 15 m electrolyte solution after 15 cycles in a full cell. No signals from possible degradation products such as those containing $-CF_3$ groups were observed, but the amounts of species generated may be below the detection limit of NMR. Notably, the dose delivered to the samples can be tuned quite easily thanks to radiolysis, enabling the detection of minor species by increasing the irradiation dose, while in the case of the electrochemistry experiments, the analysis was performed after 15 cycles. We also investigated the surface of a Mo_6S_8 electrode after 100 cycles in the 15 m solution by X-Ray Photoelectron Spectroscopy. While the results hint at the presence of LiF (as detected in the irradiated liquid by NMR, see Figure 5c), the instability of the interface layer under the X-rays prevented us from unambiguously elucidating the nature of the film. Yet, as the HER potential is almost unchanged in the different electrolyte solutions, the decrease of the H_2 production emphasizes the strong effect of kinetics factors, with likely some changes in the nature of the interphase upon increasing the molality.

Overall, the aging of the electrolytes in full cells over 15 cycles is in agreement with the results obtained by radiolysis concerning the production of H_2 and CO_2. The cycling experiments validate the trends observed by radiolysis with a decrease in H_2 evolution and a rise in CO_2 evolution upon increased salt molality. While the radiolysis and electrochemical experiments give similar results for the main gases formed, the full panel of gases and liquid degradation species observed during radiolysis were not observed under the electrolysis-based aging. This can be linked to the fact that radiation chemistry provides a significant amount of energy in a short time, exacerbating the formation of species usually formed in minority under battery operation and consequently not detected when analyzing degradation products after cycling. Moreover, one must also consider that the degradation products were only evaluated after 15 cycles, which may prove insufficient to produce enough products to be detected, apart from the major gases evolved.

Conclusions

Herein, we used radiation chemistry methods to elucidate degradation mechanisms in LiTFSI WISEs. The results indicate that the aging mechanisms depend on the molality of the salt and the interactions between water molecules and anions. Water chemistry drives the degradation process at low molality,

resulting in high H_2 production, modest CO_2 production, and other gases containing hydrogen atoms. At high molality, anion decomposition dominates the aging behavior, causing a significant reduction in H_2 production. The production of CO_2 increases with increasing molality up to 10 m before stabilizing at the highest molalities. Species characteristic of anion degradation, such as SO_2 or C_3F_8, were only detected in samples with the highest molalities. Additionally, degradation gases containing -CF_3 moieties were detected regardless of the molality value, indicating its strong influence on the degradation mechanisms. Reaction mechanisms were proposed based on the identified species, such as the formation of CF_2O as an intermediate in the CO_2 production reaction.

Picosecond-pulsed electron radiolysis was used to follow the fate of solvated electrons in these WISEs. Increasing molality causes a corresponding increase in the solvation time of the solvated electron. In a 20 m solution, solvation was completed within 400 ps, with a characteristic time of 55 ps. Moreover, the shift of the spectrum of the solvated electron to lower wavelengths when molality increased suggests an increase in the number of Li^+ cations interacting with the solvated electron.

The species obtained through radiolysis were finally compared with degradation compounds obtained through electrochemical aging for a few cycles. Electrochemical cycling measurements coupled to gas phase measurements also evidenced a H_2 formation decrease and a CO_2 formation increase while raising the molality, in agreement with the radiolysis experiments. However, the presence of minor degradation products was difficult to detect, contrary to the case of the radiation chemistry experiments. They may be formed in a too low amount to allow their detection from only a few cycles. Besides, radiolysis favors radical-radical reactions, in contrast to electrochemistry experiments.

Radiolysis allowed uncovering numerous gases and liquid degradation species, shedding light on the possible decomposition products expected in the long-term operation of LiTFSI water-in-salt electrolytes. The chemical structure of the anion or the nature and charge of the cation should affect the composition and amount of degradation products. Therefore, studying how other WISEs behave under ionizing radiation and more generally understanding how the cation and anion chemistry affect aging behavior is essential. Radiation chemistry techniques constitute, in this regard, a precious and efficient tool to study the long-term aging of batteries that is practically inaccessible by other methods.

Experimental Section

Electrolyte preparation and properties

Lithium bis(trifluoromethanesulfonyl)imide ($Li(CF_3SO_2)_2N$ (99.9%, Solvionic) LiTFSI was used as received. Aqueous electrolytes based on LiTFSI were prepared by mixing the salt (stored and precisely weighed in a glovebox under Ar) with ultra-pure water under magnetic stirring for 30 min at ambient temperature. Different samples were prepared: 1 m, 5 m, 7 m, 10 m, 15 m, and 20 m (Table 1). This latter value is just below the solubility limit of LiTFSI in water (21 m).[56] The viscosity and density of all the solutions were measured at 20 °C on a vibrating-tube densitometer (DMA 4500M, Anton Parr) coupled with a rolling-ball microviscosimeter (Lovis 2000M/ME, Anton Parr). At high molality values, proper pH measurement is challenging. Recent electrochemical measurements have suggested that the proton concentration changes by almost two orders of magnitude when the LiTFSI molality increases from 1 to 20 m.[57] Moreover, the activity of protons also changes upon the increase of the salt molality. The pH of the solution, which is roughly equal to 7 for $m=1$ decreases when m increases. The solution is slightly acidic when m is equal to 20.[57]

Electrochemistry measurements

The electrochemical stability windows (ESW) were measured using a three-electrode cell. The electrolyte solution was degassed with argon for 20 min for each measurement to remove any O_2 or CO_2 molecules. The working electrodes used were a platinum electrode (∅1.6 mm) or a glassy carbon electrode (∅3 mm). Prior to the analysis, the working electrode was mirror polished. Working and counter-electrodes were washed with ethanol and put in an ultrasonic bath for 20 min, first in ultra-pure water and then in ethanol. The counter electrode was a platinum wire (∅0.5 mm), and the reference electrode was an Ag/AgCl electrode containing a 3 M NaCl internal solution (ALS Japan, 1.95 V vs. RHE (reversible hydrogen electrode, 25 °C)).

To determine the stability limits of each system, cyclic voltammetry was performed at room temperature with a scan rate of 100 $mV\,s^{-1}$ using a BioLogic VMP3 potentiostat. The cell remained closed under argon during the experiment. The 45° tangent method was used to determine the upper and lower limits of the ESWs.

The gases produced during cycling were measured using a specially designed ampoule. The specially designed ampoule is composed, in its upper part, of a tight metallic valve allowing gas measurement (Figure S13). Two tungsten wires are embedded in the glass and extend to the bottom of the first part of the cell to hold the support grid containing the electrodes at the end. The second part, which contains the electrolyte, is attached to the upper cell by a clip and a viton ring that ensure sealing and airtightness between the two parts of the cell.

The electrodes used for cycling were $LiMn_2O_4$ (Alfa Aesar) and Mo_6S_8 (synthesized by a solid state reaction and acid etching following the protocol in Ref. [58]). They were composed of 80% active material, 10% carbon super P (Alfa Aesar) and 10 polytetrafluoroethylene (PTFE, Sigma-Aldrich). Active material, carbon and binder were mixed for a few minutes to obtain a homogeneous paste. This mixture was shaped to obtain a compact and flat electrode. It was then pressed on a stainless-steel grid of 12 mm diameter. The electrodes were kept for at least 24 h at 60 °C in an oven before cycling.

The assembly of the upper and lower part of the cell and the filling of 3 mL of the electrolyte into the ampoule were done in a glove box under an inert argon atmosphere. The ampoule was completely sealed in the glove box and kept under an inert atmosphere of about 1 bar for the total duration of cycling. Cycling was performed at C/5 rate for 15 cycles. C/rate was determined based on the active material mass of the limiting electrode.

Characterization of electrolytes by infrared spectroscopy and NMR

Infrared spectra of the electrolyte solutions were recorded with a Fourier transform infrared spectrometer (Bruker, Tensor 27). The

spectra were obtained from 50 scans with a resolution of 4 cm^{-1} in the 500–4500 cm^{-1} wavenumber range using the Attenuated Total Reflection (ATR) technique with a Golden Gate ATR accessory equipped with a diamond crystal. The background was recorded in the absence of any sample. In an ATR setup, the penetration depth of the evanescent wave depends on several parameters, and particularly on the wavelength on the beam.[59] Therefore, we made a crude correction of the ATR signal by multiplying it by the wavenumber. The O–H stretch region was decomposed with three components using a least squares method based on the data reported in Zhang et al.[14]

Liquid ^1H Nuclear magnetic Resonance (NMR) experiments on pristine samples were performed on a 400 MHz Bruker spectrometer. Each sample was prepared at ambient temperature (300 μL of sample in an insert tube containing 10 mM of NaTMSP (sodium-3-trimethylsilylproprionate) in D_2O (deuterated water)). The ^1H and ^{19}F NMR experiments on the irradiated samples were carried out on a Bruker 500 MHz NEO operating at a frequency of 499.167 and 469.647 MHz, respectively, with a 4 mm HX magic-angle probe. The ^1H and ^{19}F spectra were acquired with a single-pulse experiment using a 90° pulse of 4 and 6.25 µs, respectively, with a recycle delay of 5 s for a total of 128 transients. The magic angle sample spinning rate was set at 8–10 kHz. The ^1H and ^{19}F spectral chemical shifts were referenced to 4.8 ppm of pure H_2O and −122.0 pm of Teflon,[60] respectively.

Radiolysis experiments

Picosecond-pulsed electron radiolysis experiments

Picosecond-pulsed radiolysis experiments were performed at the laser-driven electron accelerator ELYSE.[61] The various electrolytes were bubbled with argon during these experiments to avoid any water uptake. The electron pulses were delivered with a pulse duration of about 7 ps and an electron energy of 7.6 MeV at a repetition rate of 5 Hz. Two experimental configurations were used depending on the investigated timescale. The transient absorbance of the samples was probed in a flow cell with a 5 mm optical path collinear to the electron pulse propagation. The basic optical configuration of the first experimental configuration, a pump-probe setup, allows recording signals up to 10 ns, here in the 350–720 nm spectral range. More experimental details concerning this setup can be found in reference.[62] The signals were recorded in the ns-µs time scale in the second configuration with a streak camera and a homemade repetitive flash lamp.[63] In a single experiment, spectra (in the 300–800 nm wavelength range) were obtained at given times and kinetics at various wavelengths. The precision of the measurements was about 2 mO.D. (O.D. being the optical density).

The dose per pulse was deduced from the absorbance of the hydrated electron e^-_{aq} in water, measured just before a series of experiments, as detailed in reference[62]. The dose per pulse in water was ca. 100 Gy (1 Gy = 1 J kg^{-1}) and was very stable during the day. In the concentrated aqueous solutions, the dose factor F between a pure water sample and the WISEs under study here can be calculated using Eq. (11):

$$F = \frac{\left(\frac{Z_{salt}}{A_{salt}} p + \frac{Z_{water}}{A_{water}} (100 - p)\right)}{\frac{Z_{water}}{A_{water}}^{*} 100} \quad (11)$$

with Z_{salt} (Z_{water}) the number of electrons of LiTFSI and of water, respectively; A_{salt} (A_{water}) the mass number of LiTFSI and of water, respectively and p the weight fraction of the salt, which is given in Table 1. Here, $Z_{water} = 10$; $Z_{salt} = 140$; $A_{water} = 18$ and $A_{salt} = 286$. Therefore, when the molality of the solution increases from 1 m to 20 m, F decreases from 0.97 to 0.90. This means that in all irradiation experiments, the dose received by the various electrolytes and by water alone is very similar, within a maximum 10% discrepancy.

Spectro-kinetic data analysis

The spectro-kinetics matrix consists of the absorbance values measured at different times and wavelengths. A wavelength-dependent baseline correction was applied to enable multivariate curve resolution alternating least squares (MCR-ALS) analysis by the spectro-kinetic analysis code (SK-Ana).[64,65] The number of absorbing species in a global matrix was assessed by singular value decomposition.[66] Positivity constraints were imposed for both spectra and kinetics.

Radiolysis experiments performed in order to identify the formation of stable molecules

The various electrolytes (around 1.0 mL, weighed precisely in each case) were placed in a Pyrex glass ampoule (~10 mL). The ampoule was degassed and quickly filled with 1.5 bar of ultra-pure argon (99.9999%). This operation was repeated three times in order to ensure the careful removal of air before the first irradiation step and then once between every irradiation step. Irradiation was performed using 10 MeV electron pulses of a Titan Beta, Inc. linear accelerator (LINAC). The duration of the pulse was 10 ns and the repetition rate ranged between 2 and 10 Hz. We checked carefully that no macroscopic heating of the sample took place during irradiation. The dose per pulse (20 Gy, with 1 Gy = 1 J kg^{-1}) was determined using the Fricke dosimetry.[67] The dose received by the samples was considered to be the same as the dose received by water, and no correction was applied.

Identification of the products formed upon irradiation in the gas phase

The amount of H_2, CH_4, CO and CO_2 gases, if present, were quantified by µ-GC (µ-GC-R3000, SRA instrument) using ultra-high purity argon and helium as carrier gases. Gas measurements were performed after each irradiation step. In order to assess uncertainty on the gas production measurements, the measurements were systematically repeated several times. They were found to be reproducible with an uncertainty equal to 10% at the maximum.

The nature of the gases was also obtained through gas chromatography coupled to mass spectrometry (GC-MS) with an Agilent Technologies 6890B apparatus. Argon was used between each analysis in order to clean the setup. The mass spectrometer is equipped with an electron impact source and a quadrupole mass analyzer. The mass range was 4–160. Helium was used as the vector gas with a flow rate of 2 mL min^{-1}. Separation was carried out with a CP-PorabondQ (25 m, ∅0.32 mm) column (Varian). The injector was set at 110 °C in splitless mode.

Acknowledgements

CEA is gratefully acknowledged for the PhD funding of Malaurie Paillot through CFR. We thank Christophe Fajolles for assisting in the NMR experiments. Nicholas Henry Cohen Lewis, Edward Maginn and Andrei Tokmakoff are gratefully acknowledged for kindly providing their published data for the IR spectra fitting.

The French EMIR&A network and Jean-Philippe Larbre are gratefully acknowledged for providing irradiation beam time at ELYSE platform. The French EMIR&A network and Jorge Vieira are gratefully acknowledged for providing irradiation beam time at ALIENOR platform. This work was supported by the French National Research Agency (ANR) under the Project ANR-21-CE50-0005-01. We thank Dr. Mark Levenstein for his careful reading of the manuscript and insightful comments.

Conflict of Interests

The authors declare no conflict of interest.

Data Availability Statement

The data that support the findings of this study are openly available in ZENODO at https://doi.org/10.5281/zenodo.8082589, reference number 8082589.

Keywords: concentrated aqueous electrolytes · radiolysis · electrochemistry · energy conversion · ageing

[1] K. Xu, *Nat. Energy* **2021**, *6*, 763–763.
[2] C. P. Grey, J. M. Tarascon, *Nat. Mater.* **2017**, *16*, 45–56.
[3] L. Xia, L. Yu, D. Hu, G. Z. Chen, *Mater. Chem. Front.* **2017**, *1*, 584–618.
[4] W. Li, J. R. Dahn, D. S. Wainwright, *Science* **1994**, *264*, 1115–1118.
[5] Y. Yamada, K. Furukawa, K. Sodeyama, K. Kikuchi, M. Yaegashi, Y. Tateyama, A. Yamada, *J. Am. Chem. Soc.* **2014**, *136*, 5039–5046.
[6] J. Wang, Y. Yamada, K. Sodeyama, C. H. Chiang, Y. Tateyama, A. Yamada, *Nat. Commun.* **2016**, *7*, 12032.
[7] L. Suo, O. Borodin, T. Gao, M. Olguin, J. Ho, X. Fan, C. Luo, C. Wang, K. Xu, *Science* **2015**, *350*, 938–943.
[8] Y. Yamada, K. Usui, K. Sodeyama, S. Ko, Y. Tateyama, A. Yamada, *Nat. Energy* **2016**, *1*, 16129.
[9] M. R. Lukatskaya, J. I. Feldblyum, D. G. Mackanic, F. Lissel, D. L. Michels, Y. Cui, Z. Bao, *Energy Environ. Sci.* **2018**, *11*, 2876–2883.
[10] J. Xie, Z. Liang, Y.-C. Lu, *Nat. Mater.* **2020**, *19*, 1006–1011.
[11] J. Zheng, G. Tan, P. Shan, T. Liu, J. Hu, Y. Feng, L. Yang, M. Zhang, Z. Chen, Y. Lin, J. Lu, J. C. Neuefeind, Y. Ren, K. Amine, L.-W. Wang, K. Xu, F. Pan, *Chem* **2018**, *4*, 2872–2882.
[12] N. Dubouis, P. Lemaire, B. Mirvaux, E. Salager, M. Deschamps, A. Grimaud, *Energy Environ. Sci.* **2018**, *11*, 3491–3499.
[13] Z. Li, R. Bouchal, T. Mendez-Morales, A.-L. Rollet, C. Rizzi, S. Le Vot, F. Favier, B. Rotenberg, O. Borodin, O. Fontaine, M. Salanne, *J. Phys. Chem. B* **2019**, *123*, 10514–10521.
[14] Y. Zhang, N. H. C. Lewis, J. Mars, G. Wan, N. J. Weadock, C. J. Takacs, M. R. Lukatskaya, H.-G. Steinrück, M. F. Toney, A. Tokmakoff, E. J. Maginn, *J. Phys. Chem. B* **2021**, *125*, 4501–4513.
[15] R.-S. Kühnel, D. Reber, C. Battaglia, *J. Electrochem. Soc.* **2020**, *167*, 070544.
[16] G. Ah-lung, B. Flamme, F. Ghamouss, M. Maréchal, J. Jacquemin, *Chem. Commun.* **2020**, *56*, 9830–9833.
[17] L. Droguet, A. Grimaud, O. Fontaine, J.-M. Tarascon, *Adv. Energy Mater.* **2020**, *10*, 2002440.
[18] D. Reber, R.-S. Kühnel, C. Battaglia, *ACS Materials Lett.* **2019**, *1*, 44–51.
[19] S. Le Caër, *Water* **2011**, *3*, 235–253.
[20] D. Ortiz, V. Steinmetz, D. Durand, S. Legand, V. Dauvois, P. Maître, S. Le Caër, *Nat. Commun.* **2015**, *6*, 6950.
[21] D. Ortiz, I. Jiménez Gordon, J.-P. Baltaze, O. Hernandez-Alba, S. Legand, V. Dauvois, G. Si Larbi, U. Schmidhammer, J.-L. Marignier, J.-F. Martin, J. Belloni, M. Mostafavi, S. Le Caër, *ChemSusChem* **2015**, *8*, 3605–3616.
[22] F. Varenne, J. P. Alper, F. Miserque, C. S. Bongu, A. Boulineau, J.-F. Martin, V. Dauvois, A. Demarque, M. Bouhier, F. Boismain, S. Franger, N. Herlin-Boime, S. L. Caër, *Sustain. Energy Fuels* **2018**, *2*, 2100–2108.
[23] S. F. Lux, L. Terborg, O. Hachmöller, T. Placke, H.-W. Meyer, S. Passerini, M. Winter, S. Nowak, *J. Electrochem. Soc.* **2013**, *160*, A1694–A1700.
[24] L. Coustan, G. Shul, D. Bélanger, *Electrochem. Commun.* **2017**, *77*, 89–92.
[25] T. Lv, L. Suo, *Curr. Opin. Electrochem.* **2021**, *29*, 100818.
[26] N. H. C. Lewis, B. Dereka, Y. Zhang, E. J. Maginn, A. Tokmakoff, *J. Phys. Chem. B* **2022**, *126*, 5305–5319.
[27] O. Borodin, L. Suo, M. Gobet, X. Ren, F. Wang, A. Faraone, J. Peng, M. Olguin, M. Schroeder, M. S. Ding, E. Gobrogge, A. von Wald Cresce, S. Munoz, J. A. Dura, S. Greenbaum, C. Wang, K. Xu, *ACS Nano* **2017**, *11*, 10462–10471.
[28] J. Lim, K. Park, H. Lee, J. Kim, K. Kwak, M. Cho, *J. Am. Chem. Soc.* **2018**, *140*, 15661–15667.
[29] K. Miyazaki, N. Takenaka, E. Watanabe, S. Iizuka, Y. Yamada, Y. Tateyama, A. Yamada, *J. Phys. Chem. Lett.* **2019**, *10*, 6301–6305.
[30] N. H. C. Lewis, Y. Zhang, B. Dereka, E. V. Carino, E. J. Maginn, A. Tokmakoff, *J. Phys. Chem. C* **2020**, *124*, 3470–3481.
[31] S. Bratos, J.-C. Leicknam, S. Pommeret, *Chem. Phys.* **2009**, *359*, 53–57.
[32] D. E. Moilanen, D. Wong, D. E. Rosenfeld, E. E. Fenn, M. D. Fayer, *Proc. Nat. Acad. Sci.* **2009**, *106*, 375–380.
[33] I. Rey, P. Johansson, J. Lindgren, J. C. Lassègues, J. Grondin, L. Servant, *J. Phys. Chem. A* **1998**, *102*, 3249–3258.
[34] J. W. T. Spinks, R. J. Woods, *An Introduction to Radiation Chemistry, 3rd Edition*, New York USA by Wiley, **1990**.
[35] F. Torche, J.-L. Marignier, *J. Phys. Chem. B* **2016**, *120*, 7201–7206.
[36] J. Bonin, I. Lampre, M. Mostafavi, *Radiat. Phys. Chem.* **2005**, *74*, 288–296.
[37] W. A. Narvaez, S. J. Park, B. J. Schwartz, *J. Phys. Chem. B* **2022**, *126*, 3748–3757.
[38] U. Schmidhammer, P. Pernot, V. D. Waele, P. Jeunesse, A. Demarque, S. Murata, M. Mostafavi, *J. Phys. Chem. A* **2010**, *114*, 12042–12051.
[39] H.-G. Steinrück, C. Cao, M. R. Lukatskaya, C. J. Takacs, G. Wan, D. G. Mackanic, Y. Tsao, J. Zhao, B. A. Helms, K. Xu, O. Borodin, J. F. Wishart, M. F. Toney, *Angew. Chem.* **2020**, *132*, 23380–23387.
[40] M. C. Sauer, S. Arai, L. M. Dorfman, *J. Chem. Phys.* **1965**, *42*, 708–712.
[41] F. Y. Jou, L. M. Dorfman, *J. Chem. Phys.* **1973**, *58*, 4715–4723.
[42] F. -Yuan Jou, G. R. Freeman, *J. Phys. Chem.* **1979**, *83*, 2383–2387.
[43] W. R. Dolbier Jr., *Guide to Fluorine NMR for Organic Chemists, Second Edition*, John Wiley & Sons, **2016**.
[44] Y. Ao, J. Peng, L. Yuan, Z. Cui, C. Li, J. Li, M. Zhai, *Dalton Trans.* **2013**, *42*, 4299–4305.
[45] É. Bossé, L. Berthon, N. Zorz, J. Monget, C. Berthon, I. Bisel, S. Legand, P. Moisy, *Dalton Trans.* **2008**, 924–931.
[46] B. J. Mincher, J. F. Wishart, *Solvent Extr. Ion Exch.* **2014**, *32*, 563–583.
[47] P. Tarábek, A. Lisovskaya, D. M. Bartels, *J. Phys. Chem. B* **2019**, *123*, 10837–10849.
[48] I. A. Shkrob, T. W. Marin, S. D. Chemerisov, J. F. Wishart, *J. Phys. Chem. B* **2011**, *115*, 3872–3888.
[49] Z. Jiang, D. Adjei, S. A. Denisov, M. Mostafavi, J. Ma, *Environ. Sci. Technol. Lett.* **2023**, *10*, 59–65.
[50] C. Xu, A. Durumeric, H. K. Kashyap, J. Kohanoff, C. J. Margulis, *J. Am. Chem. Soc.* **2013**, *135*, 17528–17536.
[51] A. France-Lanord, F. Pietrucci, A. M. Saitta, J.-M. Tarascon, A. Grimaud, M. Salanne, *PRX Energy* **2022**, *1*, 013005.
[52] T. Uchimaru, S. Tsuzuki, M. Sugie, K. Tokuhashi, A. Sekiya, *Chem. Phys. Lett.* **2004**, *396*, 110–116.
[53] L. Suo, D. Oh, Y. Lin, Z. Zhuo, O. Borodin, T. Gao, F. Wang, A. Kushima, Z. Wang, H.-C. Kim, Y. Qi, W. Yang, F. Pan, J. Li, K. Xu, C. Wang, *J. Am. Chem. Soc.* **2017**, *139*, 18670–18680.
[54] C. Yang, J. Chen, T. Qing, X. Fan, W. Sun, A. von Cresce, M. S. Ding, O. Borodin, J. Vatamanu, M. A. Schroeder, N. Eidson, C. Wang, K. Xu, *Joule* **2017**, *1*, 122–132.
[55] M. Metzger, C. Marino, J. Sicklinger, D. Haering, H. A. Gasteiger, *J. Electrochem. Soc.* **2015**, *162*, A1123–A1134.
[56] M. Becker, D. Rentsch, D. Reber, A. Aribia, C. Battaglia, R.-S. Kühnel, *Angew. Chem. Int. Ed.* **2021**, *60*, 14100–14108.
[57] D. Degoulange, N. Dubouis, A. Grimaud, *J. Chem. Phys.* **2021**, *155*, 064701.
[58] S.-H. Choi, J.-S. Kim, S.-G. Woo, W. Cho, S. Y. Choi, J. Choi, K.-T. Lee, M.-S. Park, Y.-J. Kim, *ACS Appl. Mater. Interfaces* **2015**, *7*, 7016–7024.
[59] S. L. Caër, S. Pin, S. Esnouf, Q. Raffy, J. P. Renault, J.-B. Brubach, G. Creff, P. Roy, *Phys. Chem. Chem. Phys.* **2011**, *13*, 17658–17666.
[60] Q. Chen, K. Schmidt-Rohr, *Macromolecules* **2004**, *37*, 5995–6003.
[61] J. Belloni, H. Monard, F. Gobert, J.-P. Larbre, A. Demarque, V. De Waele, I. Lampre, J.-L. Marignier, M. Mostafavi, J. C. Bourdon, M. Bernard, H. Borie, T. Garvey, B. Jacquemard, B. Leblond, P. Lepercq, M. Omeich, M. Roch, J. Rodier, R. Roux, *Nucl. Instrum. Methods Phys. Res. A* **2005**, *539*, 527–539.

[62] M. Puget, V. Shcherbakov, S. Denisov, P. Moreau, J.-P. Dognon, M. Mostafavi, S. Le Caër, *Chem. Eur. J.* **2021**, *27*, 8185–8194.
[63] J.-L. Marignier, V. de Waele, H. Monard, F. Gobert, J.-P. Larbre, A. Demarque, M. Mostafavi, J. Belloni, *Radiat. Phys. Chem.* **2006**, *75*, 1024–1033.
[64] C. Ruckebusch, M. Sliwa, P. Pernot, A. de Juan, R. Tauler, *J. Photochem. Photobiol. C* **2012**, *13*, 1–27.
[65] P. Pernot, **2018**, https://doi.org/10.5281/zenodo.1064370.
[66] G. H. Golub, C. F. Van Loan, *Matrix Computations*, The John Hopkins University Press, London, **1989**.
[67] H. Fricke, E. J. Hart, *Radiation Dosimetry*, Academic Press, New York, **1966**.

Manuscript received: May 12, 2023
Revised manuscript received: June 24, 2023
Accepted manuscript online: June 29, 2023
Version of record online: ■■, ■■

RESEARCH ARTICLE

Degradation mechanisms in LiTFSI/water solutions, which are well-known water-in-salt electrolytes (WISEs), are evidenced through an accelerated radiolysis approach. Aging mechanisms depend strongly on the molality of the salt and on the interactions and competition between the reactivities of water and the anions. The main aging products determined by radiolysis are consistent with the ones observed electrochemically.

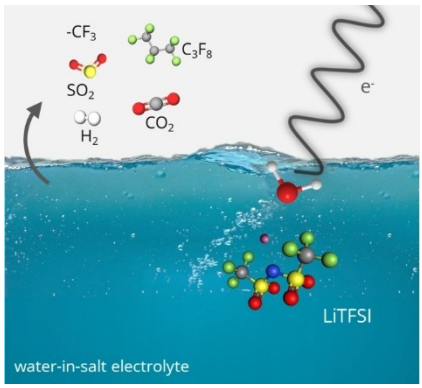

M. Paillot, Dr. A. Wong, Dr. S. A. Denisov, P. Soudan, Prof. P. Poizot, Dr. B. Montigny, Prof. M. Mostafavi, Dr. M. Gauthier, Dr. S. Le Caër**

1 – 16

Predicting Degradation Mechanisms in Lithium Bistriflimide "Water-In-Salt" Electrolytes For Aqueous Batteries